



## UvA-DARE (Digital Academic Repository)

### Modelling flow-induced vibrations of gates in hydraulic structures

Erdbrink, C.D.

**Publication date**  
2014

[Link to publication](#)

#### **Citation for published version (APA):**

Erdbrink, C. D. (2014). *Modelling flow-induced vibrations of gates in hydraulic structures*. [Thesis, fully internal, Universiteit van Amsterdam].

#### **General rights**

It is not permitted to download or to forward/distribute the text or part of it without the consent of the author(s) and/or copyright holder(s), other than for strictly personal, individual use, unless the work is under an open content license (like Creative Commons).

#### **Disclaimer/Complaints regulations**

If you believe that digital publication of certain material infringes any of your rights or (privacy) interests, please let the Library know, stating your reasons. In case of a legitimate complaint, the Library will make the material inaccessible and/or remove it from the website. Please Ask the Library: <https://uba.uva.nl/en/contact>, or a letter to: Library of the University of Amsterdam, Secretariat, P.O. Box 19185, 1000 GD Amsterdam, The Netherlands. You will be contacted as soon as possible.

## 4 Multi-scale model for discharge control and flow impact<sup>2</sup>

### 4.1 Introduction

This chapter explores the incorporation of a physics-based numerical model for simulating the local flow around the gate of a hydraulic structure in hydrodynamic flow models of a larger scale. The local flow is captured both by parametrization and simulation. The purpose of this modelling effort is twofold: (i) to investigate whether this approach can give reasonable estimates of gate discharges usable for discharge control, and (ii) use model results for judging the impact of the flow on the structure. The designation multi-scale in the chapter title refers to the fact that the local flow model runs inside a model operating at a different physical scale. No explicit links are made with research on computational aspects of multi-scale modelling.

Barrier operation is commonly based on water level predictions from system-scale far-field flow models containing river sections and sometimes coastal regions. The procedures are aimed at fulfilling the main function of the structure: for a weir in a river this is to maintain the upstream water level, for a discharge sluice this is to transfer river water out to the sea while keeping a safe inland level. Present-day hydraulic structures have various secondary functions, such as providing favourable ecological conditions, for which usually no numerical aids are available in daily operation. A better prediction of the flow near structures would be beneficial to durable performance of all barrier tasks.

Proper design studies pay attention to all functions of a structure and assess the impact of all relevant flow features. However, operational constraints change in time for natural reasons (e.g. sea-level rise) or political reasons (e.g. “Kierbesluit Haringvlietsluizen”, see Rijkswaterstaat, 2004). In addition, sometimes the design criteria that were originally applied cannot be retrieved, yielding uncertainty about safety levels and allowable limits of gate settings in the present.

There are several aspects of contemporary barrier management for which an informed view on discharge and flow properties around gates is essential. Apart from dynamic gate loads (vibrations), the prediction of bed material stability and scour, including local erosion (Hoffmans and Pilarczyk, 1995; Azamattula, 2012) as well as large-scale morphological changes of surrounding bathymetry (Nam et al., 2011) greatly depend on the flow. These aspects relate to (long-term) safety of aging structures. Additionally, ecological issues such as fish migration, salt water intrusion and mobile fauna are also linked with local flow characteristics (Martin et al., 2005). The possible impact of flow around structures on nearby

---

<sup>2</sup> This chapter uses text and content from the paper “Free-surface flow simulations for discharge-based operation of hydraulic structure gates” by C.D. Erdbrink, V.V. Krzhizhanovskaya, P.M.A. Sloot, published in January 2014 in the Journal of Hydroinformatics, Vol.16, No.1, pp.189-206, <http://dx.doi.org/10.2166/hydro.2013.215>.

shipping traffic is another feature. Above considerations motivate quantification of flow around a hydraulic structure.

There exist several non-hydrostatic CFD software options for simulating detail hydrodynamics (e.g. ANSYS-CFX, OpenFOAM, COMSOL, STAR-CD). Bollaert et al. (2012) employ numerical modelling to assess the influence of gate usage on the formation of plunge pool scour of a hydropower dam. Scheffermann and Stockstill (2009) made a transient simulation of a closing gate in a culvert of a navigation lock with STAR-CD and compared calculated pressures with physical model data. Numerous other numerical studies have looked into sluice gate flow (Akoz et al. 2009; Kim 2007; Khan et al. 2005), but transient simulations of both turbulent levels and the free surface remain challenging. Furthermore, estimating the discharge over weirs and over or under gates is not trivial. New discharge equations are still being introduced, from data-driven numerical modelling (Khorchani and Blanpain, 2005) and from physical experiments (Habibzadeh et al., 2011).

System-scale models of inland water systems simulate the flow in river branches by solving the one-dimensional or quasi-two dimensional shallow water equations, also known as Saint-Venant equations (Deltares 2012a, b). The fact that these hydrostatic models do not simulate the flow around hydraulic structures explicitly is not a severe limitation for most applications. The system effect of the operation of various gates on the water levels in adjacent water bodies (river branches) can be studied, for instance (Becker and Schwanenberg, 2012). For stability of granular bed material and salt water transport, however, the flow acceleration in the vertical dimension needs to be simulated. Moreover, the downside of primarily water level-centered validation and calibration in combination with parameterized structure representations (such as constant discharge coefficients) is that the prediction quality of discharges in system-scale models is often unclear. Warmink et al. (2007, 2008) investigated the uncertainty in calibration of water levels in river models resulting from the limited availability of discharge data. It was concluded that the necessary extrapolation of the calibration parameter (bed roughness of main channel) leads to significant uncertainty in simulated design water levels. More intensive measurement of discharges, for which most gated structures are ideal, and a physically more realistic representation of hydraulic structures in models are self-evident improvements that nevertheless require a culture shift.

The remainder of this chapter is organized as follows: first, we describe the overall approach, then the method is described in three sections about discharge modelling, free-surface flow simulation and analysis of the modelling results. Next, the results of a series of validation runs for the free-surface model are discussed, followed by results of a test case that gives numerical examples of all modelling steps. We end the chapter with recommendations, conclusions and an outlook on future work.

## **4.2 Approach and method**

### **4.2.1 General**

For obtaining a timely prediction of the flow around gates, we propose a multi-step physics-based modelling strategy which uses data input from a system-scale model. The work-flow of the suggested gate operation system is shown in Figure 4.1.

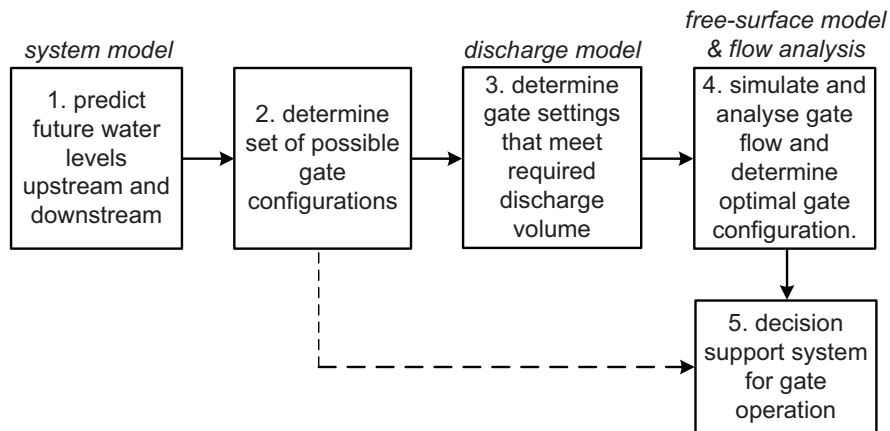


Figure 4.1. Scheme of evaluation steps leading to a decision on optimal gate operation. Steps 1-4 are treated in this chapter. The dashed line shows the shorter decision sequence taken by barrier systems that do not take into account flow effects.

The first step consists of the extraction of predicted water levels on both sides of the structure from a far-field (system-scale) model that contains the structure. Different possible gate settings (when to open, how many gates to use) are identified in the second step. All options need to be assessed in terms of discharge capacity; this happens in step 3. In the fourth step of Figure 4.1, for all gate configurations capable of discharging the required volume, the resulting flow is simulated using CFD. Subsequent analysis of the simulation results determines the impact of the flow for specific issues such as bed stability. The fifth and final step comprises the actual decision of gate operation actions. The conventional sequence of steps taken by most operational systems follows the dashed line in Figure 4.1, skipping steps 3 and 4. The present study focuses on steps 2-4, which can be seen as an addition to computational decision support systems (steps 1 and 5) by Boukhanovsky and Ivanov (2012) and Ivanov et al.(2012).

A multi-gated discharge sluice with underflow gates will be used to describe the modelling method. The central question addressed is how to find the set of gate configurations capable of delivering the required discharge that also meet the relevant constraints on flow properties.

#### 4.2.2 Configurations of multi-gated structure

Let us consider the gate configurations of a discharge structure consisting of  $n$  similar openings, each accommodating a movable gate. See Figure 4.2. In its idle state, all  $n$  gates close off the openings between the piers and the total discharge is zero. During a discharge event,  $m$  gates will be opened partially or completely, allowing a certain discharge through the structure. A 'gate configuration' is defined as the allocation of a number of gates ( $m \leq n$ ) that are opened with a gate opening  $a(t)$  while the other gates remain closed. All gates selected for opening will be operated similarly, i.e. with the same  $a(t)$ .

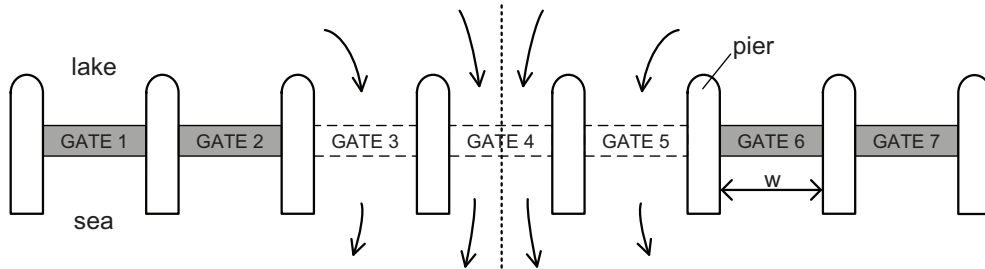


Figure 4.2. A multi-gated discharge sluice in plan view. In this example, gates 3, 4, 5 are opened, the others are closed; so  $n = 7$  and  $m = 3$ . The dotted line depicts plane of symmetry.

Before deciding which gates to open, first the possible combinations of opening gates are identified and counted. In general, flow instabilities are not favourable for maintaining an efficient and controllable discharge. As in other parts of physics, symmetry is a global measure for stability of free-surface flows. If asymmetry is allowed,  $m$  gates can be chosen freely from the total of  $n$  available slots. Then the number of possible combinations is obviously  $\binom{n}{m}$ , using the common notation for combinatorial choice of  $m$  objects out of  $n$ . For the condition of symmetry to hold, gates may only be opened in such a way that the pattern is symmetric about the vertical plane of symmetry in flow direction (see Figure 4.2). This implies that the number of options reduces to  $\binom{\lfloor n/2 \rfloor}{\lfloor m/2 \rfloor}$  for all  $0 \leq m \leq n$ , where  $m$  cannot be chosen odd if  $n$  is even – in which case there are no options at all.

For a structure with seven gates ( $n = 7$ ), for instance, the total number of possible ways to open 1, 2, ..., 7 gates is  $\sum_{i=1}^7 \binom{7}{i} - 1 = 2^7 - 1 = 127$  if asymmetry is allowed and  $\sum_{i=1}^7 \binom{\lfloor 7/2 \rfloor}{\lfloor i/2 \rfloor} = 2^{\lfloor 7/2 \rfloor} - 1 = 15$  if only symmetric configurations are permitted.

This shows that the symmetry constraint greatly reduces the number of ways to open a given number of gates. Furthermore, an even number of gates has roughly half the number of possibilities, because opening any odd number of gates then results in asymmetric inflow. This could also hold for an odd-numbered gate structure which misses one (or any odd  $m < n$ ) of the gates due to maintenance or operational failure.

#### 4.2.3 System model and gate control

The basis is formed by a classic box model, see e.g. Stelling and Booij (1999). The focus is on submerged flow through a multi-gated outlet barrier that blocks seawater from entering the lake at high tide and discharges river water to sea at low tide, see Figure 4.3. This basic model serves in the present study as a surrogate system-scale model. The water levels it generates will be used as boundary conditions for the near-field modelling.

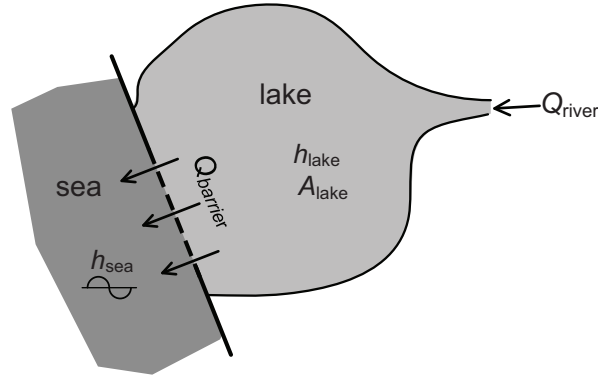


Figure 4.3. Classic box model of outflow of a river to sea. An outlet barrier structure regulates the lake level while keeping salt seawater out.

Assuming barrier gates are closed (except when discharging under natural head from lake to sea) and assuming zero evaporation and precipitation, the system is described by:

$$Q_{\text{river}} - Q_{\text{barrier}} = A_{\text{lake}} \frac{dh_{\text{lake}}}{dt}, \quad (4.1)$$

where  $Q_{\text{river}}$  is discharge from a river,  $Q_{\text{barrier}}$  is the total discharge through the gates of the barrier,  $h_{\text{lake}}$  is the water level in the lake,  $A_{\text{lake}}$  is the area of the lake assumed independent of  $h_{\text{lake}}$ . Submerged flow past an underflow gate is by definition affected by the downstream water level. As Section 4.2 described, the associated discharge depends on both water levels (sea and lake), the gate opening  $a$  and a discharge coefficient for submerged flow  $C_D$  that includes vertical contraction effect. The discharge  $Q$  through a barrier gate at time  $t$  is written as

$$Q_{\text{gate}}(t) = C_D a_i(t) w \sqrt{2g(h_{\text{lake}}(t) - h_{\text{sea}}(t))}, \quad (4.2)$$

where  $w$  is the flow width (see Figure 4.2) and the subscript “barrier” is dropped from now on. Sea level  $h_{\text{sea}}$  is approximated by a sine function. The total discharged volume that passes the barrier in the period during which  $h_{\text{lake}} > h_{\text{sea}}$  is found after summing over all  $m$  gates and integrating with respect to time.

Two gate opening scenarios will be considered. In both scenarios equal gate openings  $a(t)$  are applied to all  $m$  gates selected for opening. The first scenario uses a constant gate opening  $a_{\text{const}}$  for the whole discharge period (from  $t_{\text{start}}$  to  $t_{\text{end}}$ ). The opening required to lower the lake level to a desired lake level  $h_{\text{target}}$  is found by estimating the average required discharge  $Q_{\text{tot,req}}$  to achieve this and by making estimates of the average discharge coefficient and water levels during the discharge period:

$$a_{\text{const}} = \frac{\bar{Q}'_{\text{tot,req}}}{m\bar{C}'_D w \sqrt{2g(\bar{h}'_{\text{lake}} - \bar{h}'_{\text{sea}})}} \text{ with } \bar{Q}'_{\text{tot,req}} = \frac{A_{\text{lake}}(h_{\text{lake},t(\text{start})} - h_{\text{target}})}{t'_{\text{end}} - t_{\text{start}}}, \quad (4.3)$$

where bars are time-averages and primes indicate predictions of future values. In the second scenario, the discharge is regulated by a proportional integral derivative (PID) controller (Brown, 2007). The goal of this scenario is to have a more constant gate discharge by varying the gate openings in time, whilst still achieving the same  $h_{\text{target}}$  as in the first scenario. The discrete PID formula for discharge at  $t_i$  is

$$Q(t_i) = K_P e(t_i) + K_I \sum_{j=1}^i e(t_j) + K_D \frac{e(t_i) - e(t_{i-1})}{\Delta t}, \quad (4.4)$$

where  $K_i$  are the gain parameters and the error value is defined as  $e(t_i) = Q_{\text{set}} - Q(t_{i-1})$ . In the simulations,  $K_P = 0.10$ ,  $K_I = 0.45$  and  $K_D = 0.55$  are used. The setpoint  $Q_{\text{set}}$  is constant and equal to  $Q_{\text{tot,req}}$ , except for linear setpoint ramping applied at the start of discharge to prevent undue fluctuations of gate position. At each time step, the required gate opening is derived from this discharge divided by  $mC'_D w \sqrt{2g(h_{\text{lake}}(t) - h_{\text{sea}}(t))}$ . Figure 4.4 captures the flow chart of the system model. It includes computations of the two gate operation scenarios.

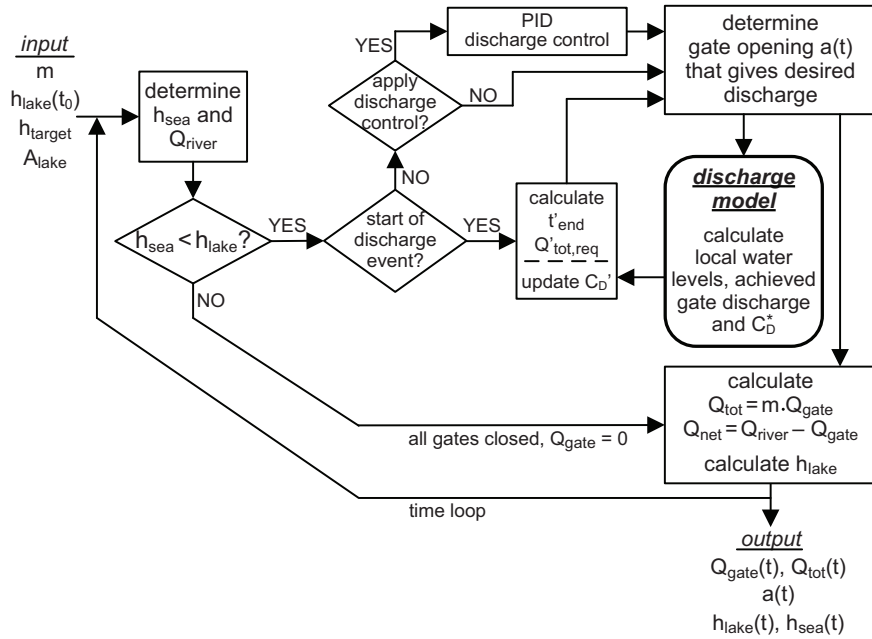


Figure 4.4. System model: flow chart of gate control and water level computations.

Figure 4.4 shows that the total discharge computed by the system model  $Q_{\text{tot}}$  is being used to calculate the new lake level. Additionally, it shows that at the start of each discharge event,

i.e. when the gates are opened, the prediction of the discharge coefficient  $C_D'$  is updated using data from the discharge model. For both situations, with and without PID control, this coefficient is found by a relaxation formula with the mean discharge coefficient  $C_D^*$  of the previous discharge event computed by the discharge model. For the  $n$ -th discharge event the update formula reads

$$C_D'(n) = C_D'(n-1) + \beta \{C_D^*(n-1) - C_D'(n-1)\} \quad (4.5)$$

In all computations a relaxation factor  $\beta = 0.75$  is applied. Discharge coefficients actually depend on numerous factors. Also, flows through neighbouring gates influence each other. To distinguish between different gate configurations with the same total flow-through area  $m \cdot w \cdot a_{const}$ , these two things need to be taken into account. This is done in the discharge model described in the next subsection, see also the bold block in Figure 4.4.

#### 4.2.4 Discharge model

Vertical lift gates with underflow are raised vertically between piers of a structure. When the gates are lifted higher than the water surface, there exists free or submerged Venturi flow (Boiten, 1994). These flow types have different discharge characteristics and associated formulae. For estimating the submerged flow discharge with a partly lowered gate, the local water depths are schematized according to Figure 4.5 (after Kolkman, 1994).

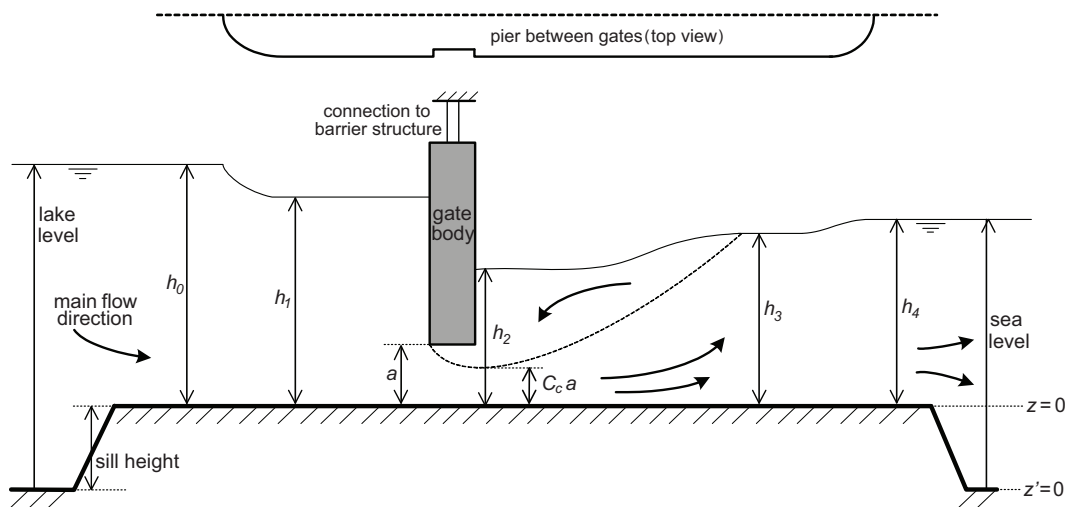


Figure 4.5. Definitions of local water depths  $h_i$  for underflow gate in hydraulic structure, after Kolkman (1994). Above: top view of pier; below: cross section free water surface around gate. Sketch not to scale.

Bernoulli's equation and the momentum balance together give a system of four equations. Each equation is denoted  $[h_i, h_{i+1}]$  and describes the transition from water level  $h_i$  to  $h_{i+1}$  ( $h_{i+1}$  being located downstream of  $h_i$ ), in line with Figure 4.5.

$$[h_0, h_1]: h_0 + \left(\frac{Q}{w_0 h_0}\right)^2 / 2g = h_1 + (1 + \xi_{in}) \left(\frac{Q}{w h_1}\right)^2 / 2g$$

$$[h_1, h_2]: h_1 + \left(\frac{Q}{w h_1}\right)^2 / 2g = h_2 + \left(\frac{Q}{w C_c a}\right)^2 / 2g$$

$$[h_2, h_3]: \frac{1}{2} \rho g w h_2^2 + \frac{\rho Q^2}{w C_c a} = \frac{1}{2} \rho g w h_3^2 + \frac{\rho Q^2}{w h_3}$$

$$[h_3, h_4]: h_3 - h_4 = \frac{U_4^2}{2g} + (\xi_{out} - 1) \left(\frac{Q}{w h_3}\right)^2 / 2g$$

$$\text{where } \xi_{in} = \left(\frac{1}{C_{c,in}} - 1\right)^2 \text{ with } C_{c,in} = 0.025(m - 1) + 0.6 \quad (4.6)$$

These equations are solved from their polynomial forms, which works because the smallest positive root gives the desired water level in each case. In order of computation in the discharge model, these forms are:

$$h_1^3 + \left\{ h_0 + \left(\frac{Q}{w_0 h_0}\right)^2 / 2g \right\} h_1^2 + (1 + \xi_{in}) \left(\frac{Q}{w}\right)^2 / 2g = 0$$

$$h_{2,forward} = h_1 + \left(\frac{Q}{w h_1}\right)^2 / 2g - \left(\frac{Q}{w C_c a}\right)^2 / 2g$$

$$h_3^3 - \left\{ h_4 + \frac{U_4^2}{2g} \right\} h_3^2 + (1 - \xi_{out}) \left(\frac{Q}{w}\right)^2 / 2g = 0$$

$$\frac{1}{2} \rho g w h_{2,backward}^2 + \frac{\rho Q^2}{w C_c a} - \frac{1}{2} \rho g w h_3^2 - \frac{\rho Q^2}{w h_3} = 0. \quad (4.7)$$

These polynomials are solved for  $0 < Q \leq Q_{MF}$ . The constraint  $h_{2,forward} = h_{2,backward}$  may be solved graphically, yielding the actually achieved discharge. Transitions  $h_0-h_1$  and  $h_3-h_4$  with loss coefficients  $\xi_{in}$  and  $\xi_{out}$  represent the effects of flow entering and leaving the narrow area between two piers. Transitions  $h_1-h_2-h_3$  are the characteristic underflow gate zones. Computations were carried out according to the flow chart in Figure 4.6. The lake and sea levels computed in the system model served as boundary conditions - for variables  $h_0$  and  $h_4$  of this model, respectively.

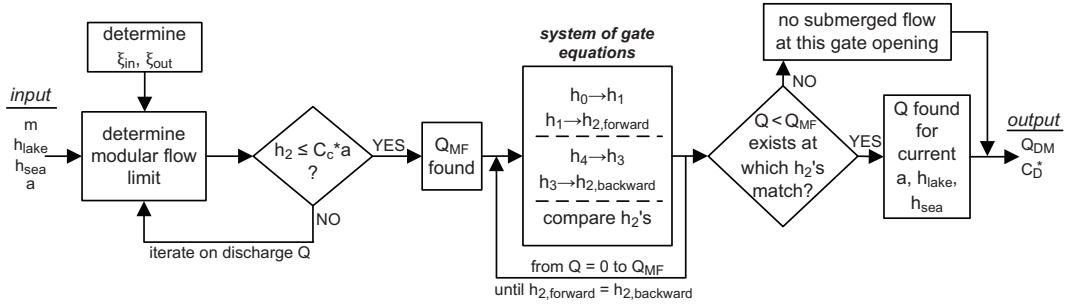


Figure 4.6. Flow chart of discharge model. This computation is repeated each time step; it is fully contained in the block named “discharge model” in Figure 4.4.

A good geometric design of a discharge-regulator is such that no transition occurs from one flow type to another during regular usage. The model therefore checks if indeed submerged discharge occurs. As criterion for reaching the modular flow discharge  $Q_{MF}$ , the minimum flow depth in the control section  $h_2$  is compared to the flow height in the point of maximum vertical contraction  $C_c \cdot a$ . Free and intermediate flow regimes are thus detected, but are not being calculated. Submerged Venturi flow is not considered either, since the idea is to actively *control* the flow.

All four non-linear equations are reshaped into third-order polynomials  $f(h_i, h_{i+1}, Q) = 0$ . Discharge  $Q$  is substituted for the velocity terms and remains as the only unknown in the system of equations. As prescribed for sub-critical flow conditions (Chow, 1959), computational direction behind the gate is from downstream to upstream ( $h_4$  to  $h_2$ ). On the lake side, computations go in flow direction up to the control section ( $h_0$  to  $h_2$ ). The discharge coefficient  $C_D$  is derived from the contraction coefficient  $C_c$  for sharp-edged gates, fitted on experimental data cited in Kolkman (1994) so that the full range of gate openings  $a/h_1$  is covered. Combining two empirical formulations, the contraction coefficient for sharp-edged gates is assumed equal to:

$$C_c = \frac{0.782}{1.782 - a/h_1} \text{ for } \frac{a}{h_1} > 0.5 \text{ (regime Henry, 1950) and}$$

$$C_c = -0.004 \log(a/h_1) + 0.6074 \text{ for } \frac{a}{h_1} \leq 0.5 \text{ (regime Cozzo, 1978).} \quad (4.8)$$

Iterations on  $Q$  ultimately yield a value at which  $h_{2,forward}$ , computed from upstream, is equal to  $h_{2,backward}$  computed from downstream. This is the achieved value of  $Q$  for the given gate opening  $a$ . The entrance and exit losses are assumed to depend on the number of gates in use ( $m$ ). The method does not distinguish between different gate configurations with equal  $m$ , however. Numerical results are shown in the results section.

### 4.3 CFD simulations

Step 4 in Figure 4.1 consists of two parts: free-surface CFD simulations, called “Model I” in Table 3.1 and discussed in Section 4.4.1; and flow impact analysis, discussed in Section 4.4.2.

#### 4.3.1 Model set-up

A non-hydrostatic flow model is applied to find out which of the selected gate settings is most favourable in terms of flow properties. The two-dimensional domain is defined by a vertical cross section through the gate section (abbreviated as 2DV) from a lake to the sea, see Figure 4.8. A rigid rectangular gate with a sharp-edged bottom is modelled implicitly by cutting its shape out of the flow domain. The Reynolds-Averaged Navier-Stokes (RANS) equations for incompressible flow are the basis for the simulations. These will be given in Chapter 6. Figure 4.7 gives the flow chart of the CFD simulations. The model domain covers the flow from  $h_1$  to  $h_3$ . These input values are taken from the discharge model.

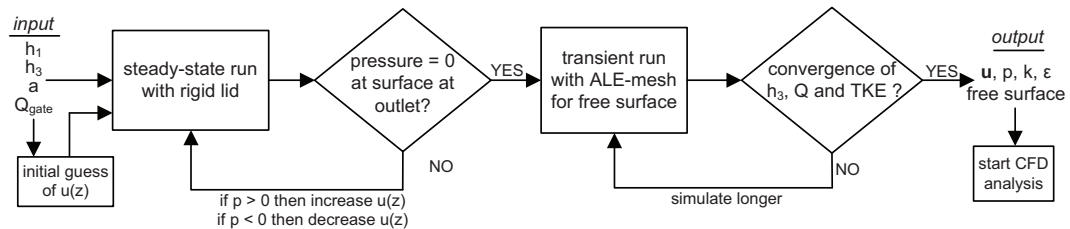


Figure 4.7. Flow chart of FEM free-surface flow simulations.

For each simulated flow situation two consecutive runs are made: a steady-state run and a time-dependent transient run. In the former run, iterations on the outflow velocity profile are done until pressure at the surface becomes zero. The results of this pre-run are then implemented as initial conditions for the transient run, which uses a moving mesh to simulate the free surface. Boundary conditions are similar for both runs except for the surface downstream of the gate, see Figure 4.8.

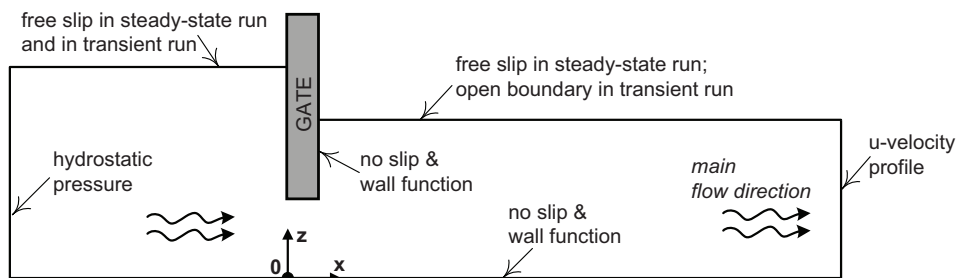


Figure 4.8. Boundary conditions of CFD model. The main flow direction is from left to right. Not drawn to scale.

The upstream flow boundary consists of a hydrostatic pressure profile  $p(z) = \rho g(h_1 - z)$ . The downstream boundary is a block profile  $u$ -velocity. No slip is applied at the walls ( $\mathbf{u} = 0$ ) along with a wall function. The steady pre-run uses a ‘rigid lid’ (free slip boundary,  $\mathbf{u} \cdot \mathbf{n} = 0$ )

for the downstream water surface. The upstream free surface is modelled as a rigid lid in both runs.

An unstructured computational mesh is used with refinements near the bottom wall and gate boundaries, made up of around 35,000 triangular elements and yielding about 230,000 degrees of freedom for a transient run. The Arbitrary Lagrangian-Eulerian (ALE) method, see previous chapter, is used to compute the deformation of the computational mesh. Winslow smoothing (Donea et al., 2004) is applied to find the location of the inner nodes. Figure 4.9 shows part of the mesh. At the top boundary in the transient run, the velocity condition is an open boundary with zero stress in normal direction. At the same boundary the mesh velocity in normal direction is prescribed as  $u_{\text{mesh},n} = u \cdot n_x + w \cdot n_z$  (Ferziger and Perić, 2002). Mesh convergence tests showed that the applied mesh is sufficiently dense so that results do not improve on further mesh refinement.

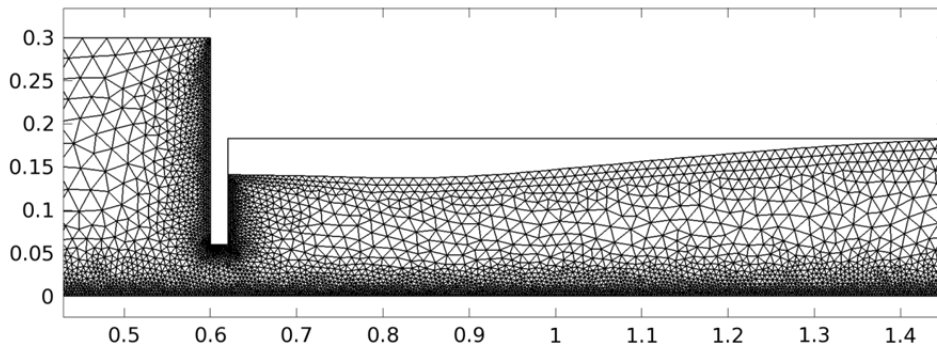


Figure 4.9. Example snapshot showing part of the computational mesh. A deformed free surface boundary downstream of the gate is visible. Flow is from left to right, units in meters.

The more common choice of applying a velocity condition upstream and a pressure boundary downstream conflicts with the required ALE moving mesh condition at the outlet boundary. Vertical mesh freedom is necessary for the surface movement. A hydrostatic pressure profile cannot be prescribed at the outlet, since any change in water depth at this boundary would imply a change of local pressure, which contradicts the applied pressure profile.

In the course of the transient run, the free surface adapts to the pressure field and vice versa. Because the physical flow situation is quasi-steady, with fluctuations depending on degree of submergence and gate opening, the surface may show oscillations in time in its equilibrium state. As a consequence the flow discharge is also not strictly constant in the equilibrium state.

The package COMSOL Multiphysics (version 4.2) is used to simulate the gate flow (COMSOL, 2013). This finite element method (FEM) solver is applied to solve the discretised RANS equations. The generalized alpha time-implicit stepping method is applied to ensure Courant stability, with a strict maximum time step of  $\Delta t = 0.02\text{s}$ . The time step in the CFD model is completely independent of the time step in the system model and discharge model. The

variables are solved in two segregated groups using a combination of the PARDISO solver and the iterative BiCGStab solver in combination with a VANKA preconditioner. The standard  $k-\varepsilon$  model is used for turbulence closure. Simulation of 24 seconds of physical time took around six hours of wall-clock time on Intel 8-core i7 processor, 2.93 GHz, 8 Gb RAM, occupying on average 1 Gb RAM and 50% of total CPU power.

### 4.3.2 Analysis of simulation output: flow impact

The second part of step 4 in Figure 4.1 is the post analysis of the modelling results obtained in previous steps. Three aspects are discussed: flow parameters, vibrations and bed stability.

#### *Flow parameters*

Three parameters that are required for assessing various types of flow impact are extracted from the CFD model: the contraction coefficient  $C_c$ , the velocity in the vena contracta  $U_{vc}$  and the Froude number  $Fr$ . The flow field is interpolated to a regular grid, so that the edge of the separated layer is found, see Figure 4.13. The contraction coefficient is thus found directly.

The cross-sectional averaged velocity in the vena contracta defined by a spatial average in the separated shear zone, is a function of time here:

$$U_{vc}(t) = \frac{1}{C_c(t)a} \int_{z=0}^{C_c(t) \cdot a} U(z, t) dz, \quad (4.9)$$

where  $U$  is the velocity magnitude scalar at the point of maximum flow contraction. For gate flow with significant fluctuations, the temporal mean of this quantity,  $\bar{U}_{vc}$ , may be used. The Froude number  $Fr$  is used as an aid for finding the transitions to intermediate and free flow regimes. It is considered time-dependent too:

$$Fr(t) = \frac{U_{vc}(t)}{\sqrt{gh_2(t)}}, \quad (4.10)$$

in which obviously  $h_2 = C_c \cdot a$  in fully free flow. An overview of critical flow theory from a historical perspective is given by Castro-Orgaz and Hager (2010) and from a more practical viewpoint by Boiten (1994). In a more complete flow assessment, not only the vertical contraction caused by the underflow gate is used as a criterion for modular flow, as is done here, but also contraction caused by horizontal and possibly vertical flow domain transitions at the inlet of the structure should be included.

#### *Vibrations*

As a simple estimating factor for occurrence of FIVs, a time-dependent version of the reduced flow velocity  $V_r$  (Section 2.4) is introduced:

$$V_r(t) = \frac{U_{vc}(t)}{f_{gate}(t) \cdot D}, \quad (4.11)$$

where  $f_{gate}$  is the response frequency of the structure in Hz;  $D$  is the gate thickness. The best option to find the gate frequency is to measure it in situ by installing sensors. An elaboration

of this idea is discussed in Chapter 7. In a first, crude estimate of the risk of a vibration initiating, it can be assumed that the amplitude  $A$  due to FIV is a function of  $V_r$ ,  $a$  and the lower water level:  $A = f(V_r, a, h_3)$ .

#### *Scour and bed protection*

The classical prediction of local scour downstream of weirs and sluice structures caused by outlet currents is described by Breusers (1966) and Hoffmans and Pilarczyk (1995). More recently, contemporary computational techniques were introduced for scour estimation, e.g. Azmathullah et al. (2006). In the classical physics-based design formulae, turbulence parameters are used to predict the depth of the scour hole in unprotected beds. For beds protected with granular material (loose rocks), the Shields parameter is a classic non-dimensional measure applied as a first indicator for instability (Shields 1936). An adapted version of this parameter used by Jongeling et al. (2003) and elaborated upon by Hofland (2005) and Hoan et al. (2011) is defined as

$$\Psi(x) = \frac{\langle (\bar{U}(x) + \alpha\sqrt{k(x)})^2 \rangle}{\Delta g d(x)} \quad \text{with } \Delta = \frac{\rho_s - \rho_w}{\rho_w}. \quad (4.12)$$

where  $\langle \dots \rangle$  denotes spatial averaging over the whole water depth,  $k$  is the turbulent kinetic energy (TKE),  $d$  is the local water depth,  $\bar{U}$  is the mean flow velocity magnitude and  $\alpha$  is an empirical parameter for bringing into account the turbulence (that depends on flow type and local geometry, e.g. slopes in bottom profile).

#### **4.4 Model validation**

A series of validation runs was done for the free-surface model. ‘Validation run’ is used here in the meaning discussed by Stelling and Booij (1999): the uncalibrated model is run without any tweaking of parameters to see if it can reproduce the most important physical features. Experimental laboratory data by Nago (1978, 1983) for a vertical sharp-edged gate under submerged efflux serve as comparison. Nago’s (1978, 1983) dimensions were used without any scaling. His discharge formula  $Q = C_E a w \sqrt{2gh_1}$  does not contain the downstream level  $h_3$  explicitly. Its influence is instead incorporated in  $C_E$ . The two coefficients are connected through

$$C_E = \frac{Q_{\text{gate}}}{a w \sqrt{2gh_1}} = C_D \sqrt{\frac{h_1 - h_3}{h_1}}, \quad (4.13)$$

The simulated discharge is computed by spatial integration of horizontal velocity at the outflow boundary. In Figure 4.10 coefficient  $C_E$  is plotted for different series of dimensionless gate openings and for a range of dimensionless downstream levels.

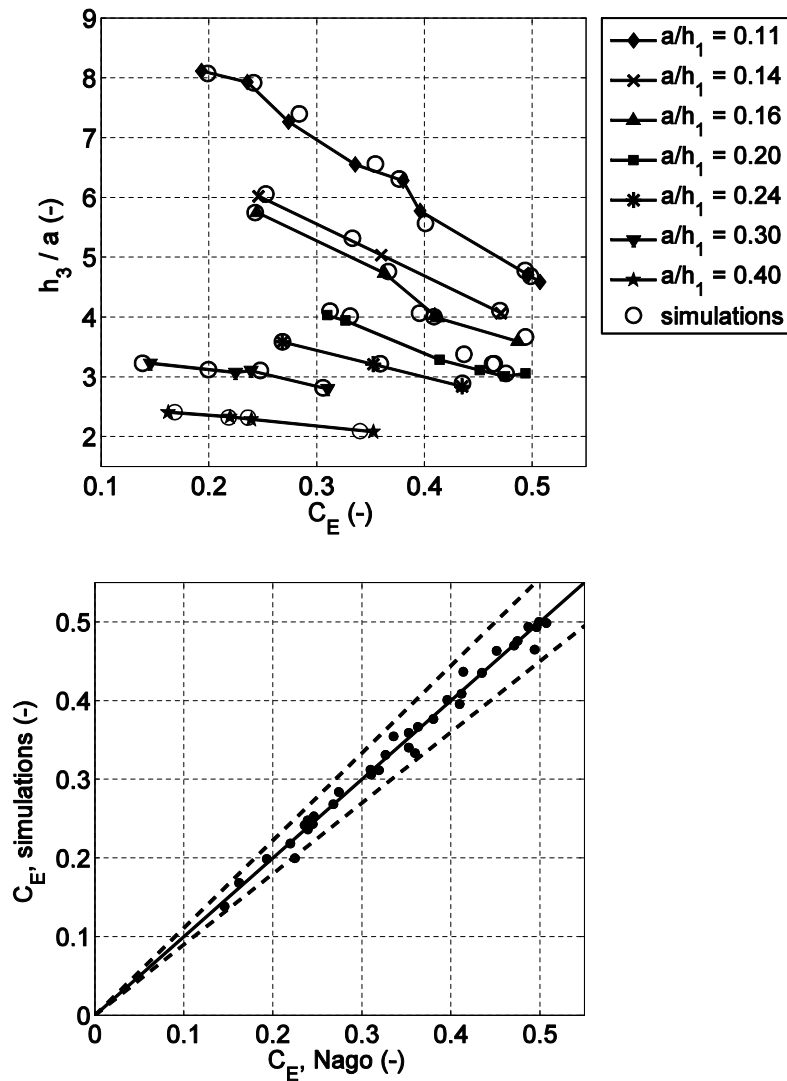


Figure 4.10. Results of validation runs showing discharge coefficient  $C_E$  simulated by the free-surface CFD model versus experimental data of submerged flow of a sharp-edged underflow gate by Nago (1978, 1983). Above: Sorted by gate opening ( $a/h_1$ ) and downstream level ( $h_3/a$ ). Below: direct comparison of the same data. Dashed lines mark 10% deviation.

The results of the validation runs make clear that the simulations capture the discharges of the experimental data quite accurately: the correlation coefficient is 0.994 and the root mean square error is 1.14%. The fact that the uncalibrated model shows good discharge estimates gives confidence in the predictive power of this modelling approach. Physical output not validated here (such as TKE) may be calibrated in future studies by adjusting suitable model parameters. Convergence of various flow variables occurs at different rates. First, the mean

velocities stabilize, and then the forces on the gate converge, then the discharge, and lastly the turbulent energy.

The chosen boundary conditions proved to lead to stable results for all submergence ratios of Nago's (1978, 1983) data. It was found that the moving mesh is the critical factor for numerical stability. ALE is a suitable method for computing the free surface for quasi-steady gate flow as long as the flow remains submerged. Steep surface gradients associated with lowering  $h_3$  cause inverted mesh elements and hence numerical instabilities.

#### **4.5 Results of test case simulations**

The described methods are illustrated by a test case example. The results of three modelling steps are discussed: the sluice model containing the system model (for water levels) plus the discharge model (Figures 4.4 and 4.6), the free-surface model (Figure 4.7) and analysis of vibrations and bed stability. Four tidal cycles and four discharge events were modelled for a discharge sluice with seven gates regulating a lake with constant river inflow. The goal is to determine the optimal number of gates to open and the best gate operation scenario.

##### **4.5.1 Results of system and discharge model**

###### *Model parameters*

- $n = 7, m = 1, \dots, 7$
- $A_{\text{lake}} = 1.9 \cdot 10^7 \text{ m}^2$
- $Q_{\text{river}} = 100 \text{ m}^3/\text{s}$
- $h_{\text{lake}}(t=0) = 6.1 \text{ m}$
- $h_{\text{target}} = 6.0 \text{ m}$
- $w = 22.5 \text{ m}$
- sill height: 3 m
- mean sea level =  $z' + 6.1 \text{ m}$
- tidal amplitude = 0.60 m
- tidal period = 12.5 hours

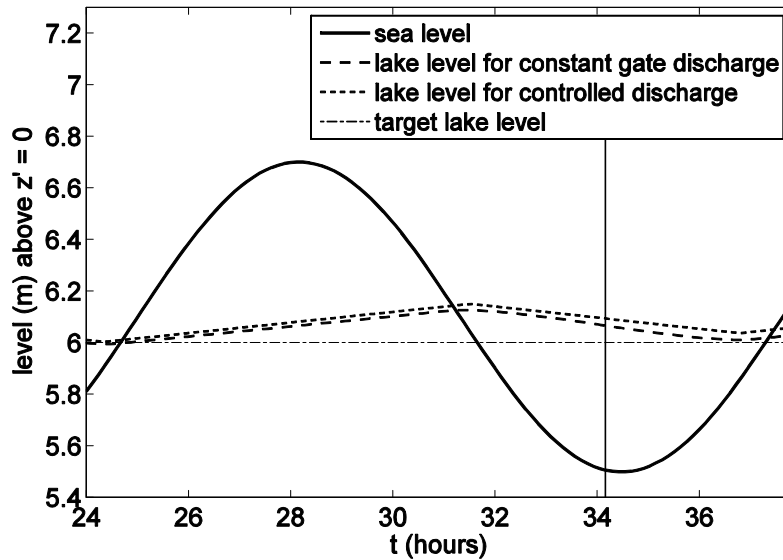


Figure 4.11. Results of sluice model for  $3 \leq m \leq 7$ : sea and lake level for gate operation scenario with and without PID-controlled discharge. Vertical line indicates moment of maximum head difference.

The sluice model was run for  $1 \leq m \leq 7$ . When opening only one gate, the target lake level could not be reached even when lifting the gate completely. When using two gates, the target level is reached, but the modular flow limit is exceeded for the greatest part of the discharge period. This results in unwanted transitions to intermediate and free flow with fluctuating discharges that are hard to control. For  $3 \leq m \leq 7$  strictly submerged flow exists and the target is met. Therefore, only these configurations are modelled further. The water levels (plotted for one cycle in Figure 4.11) show that the lake level fluctuates in a controlled way and nearly identically for the scenarios with and without discharge control. Note that the target lake level indicates not a desired average level, but the level where we want the lake to be at the end of a discharge event. In the case of Figure 4.11 it is reached exactly around  $t = 24.5$  h, and both discharge methods are slightly above the target at the end of the next event around  $t = 37.0$ h.

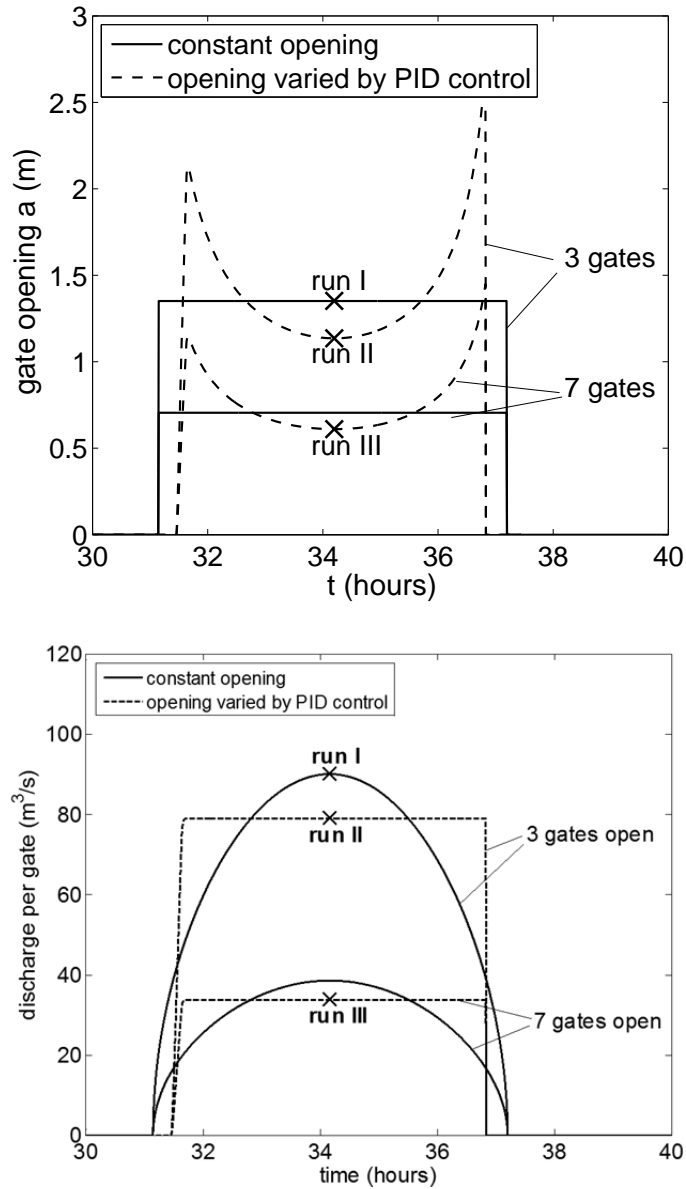


Figure 4.12. Results of sluice model for using three gates and seven gates: gate openings (upper plot) and achieved discharges per gate (lower plot).

In Figure 4.12, the gate openings and achieved gate discharges in time are plotted for one tidal period for the situations with three or seven gates opened during the discharge event. Intermediate numbers of operated gates ( $4 \leq m \leq 6$ ) lie between the shown curves for  $m = 3$  and  $m = 7$ , but are not plotted for clarity. It can be seen that constant gate openings give discharges that vary in time following the time-dependent hydraulic head difference. In the

PID-controlled scenario, the gate opening is automatically operated in such a way that the discharge stabilizes quickly after the start.

In this multi-scale modelling approach, averaged values from the discharge model are used to improve discharge predictions at system scale. However, instantaneous discharges and gate openings computed in both models inevitably differ. Largest discrepancies are around 10%. This could be improved by examining different update methods, at the cost of longer computation time.

Three configurations are selected for evaluation by free-surface simulations. These cases are marked in Figure 4.12 as runs I, II and III. Runs I and III represent extremes: a constant gate opening with only three gates in use (high  $Q$ ) and a controlled opening with all seven gates in use (low  $Q$ ). All three runs are at the time of maximum head difference. In real-life practice, more cases could be selected for simulation depending on specific interests and available computing power.

#### 4.5.2 Results of CFD simulations

To simulate the two selected runs I and II within the validated range, the levels and opening are scaled down with length scale 1:10, see Table 4.1.

Table 4.1. Values of selected CFD runs.

run	gate configuration	length scale	$h_0$ (m)	$h_1$ (m)	$h_3$ (m)	$h_4$ (m)	gate opening $a$ (m)
I	m = 3, constant opening	1:1	3.07	2.93	2.38	2.50	1.30
		1:10	0.307	0.293	0.238	0.250	0.130
II	m=3, PID control	1:1	3.07	3.00	2.44	2.50	1.14
		1:10	0.307	0.300	0.244	0.250	0.114
III	m = 7, PID control	1:1	3.07	3.06	2.49	2.50	0.610
		1:10	0.307	0.306	0.249	0.250	0.0610

input values for CFD runs.

All water levels  $h_i$  are relative to  $z = 0$ .

Table 4.1 (Continued).

run	total discharge $Q_{tot}$ ( $m^3/s$ )	discharge per gate $Q_i$ ( $m^3/s$ )	discharge per gate, per unit width $q_i$ ( $m^2/s$ )
I	270	90.1	4.00
	0.855	0.285	0.127
II	237	79.02	3.51
	0.750	0.250	0.111
III	237	33.86	1.51
	0.750	0.107	0.0476

The near-gate flow velocities, pressures, TKE and dissipation are simulated. Figure 4.13 shows a plot of the simulated flow field of run II (at length scale 1:10) by indicating  $\vec{u}$ .

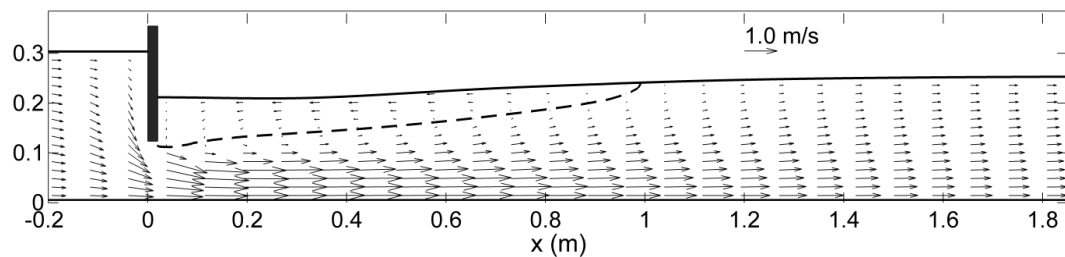
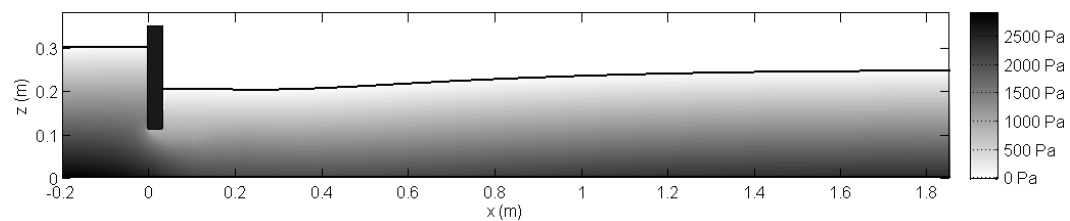


Figure 4.13. Vector flow field of run II. Flow is from left to right. The computed free surface behind the gate shows local lowering. Dashed line indicates separation between positive and negative  $u_1$ -velocity. The figure shows only part of the actual computational domain. Total domain length is 3.6 m.

The simulated free surface as expected sinks in the region directly downstream of the gate (solid line in Figure 4.13). In this case, the vena contracta is located at short distance downstream of the flow separation point. The separation between positive and negative horizontal velocities in the recirculation area is derived (dashed line in Figure 4.13). At a distance of around five times the downstream water level past the gate, the flow reattaches at the surface and the velocity starts to return to a more uniform profile.

Figure 4.14 shows plots of the pressure and turbulent kinetic energy of run II.



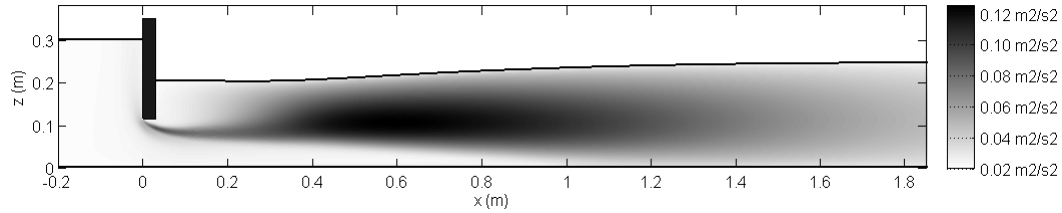


Figure 4.14. Pressure  $p$  in Pa (above) and turbulent kinetic energy  $k$  (TKE) in  $\text{m}^2/\text{s}^2$  (below) of run II.

In the case shown in the plots, the equilibrium state reached in the simulations is fully steady. Pressure gradients are mild; the pressure returns smoothly to a hydrostatic shape as the streamlines become parallel downstream. The TKE reaches a maximum in the middle of the water column at about two times the downstream water depth past the gate. Run I has a steeper surface behind the gate than run II (shown in Figures 4.13 and 4.14) and higher TKE levels, while run III has the lowest TKE levels and the most level surface downstream of the gate.

#### 4.5.3 Results of flow analysis

The output of the CFD free-surface model is used for computing the values of the three flow parameters that were discussed in an earlier section, see Table 4.2.

Table 4.2. Computed flow parameters derived from CFD model results.

run	$C_c$ (-)	$U_{vc}$ (m/s)	$Fr$ (-)
I	0.88	3.56	0.83
II	0.86	3.50	0.78
III	0.84	2.74	0.57

Table 4.2 shows that the contraction coefficients do not differ much, which is expected for similar gate types. The velocity in the control section  $U_{vc}$  is highest for the situation with highest discharge per gate (run I) and lowest for the situation with smallest discharge per gate (run III). The same holds for the Froude number. This matches observations from the free surface curvatures of the final solution of the transient simulations.

The flow impact on the bed protection material is estimated by computing  $\Psi$  for two different  $\alpha$  for the selected runs, see Equation (4.12). Variation of  $\alpha$  controls the relative contribution of turbulent kinetic energy to the flow impact. The whole water depth  $d$  is used for averaging the square of the maximum local velocity term  $(\bar{U} + \alpha\sqrt{k})^2$ . The results are plotted in Figure 4.15.

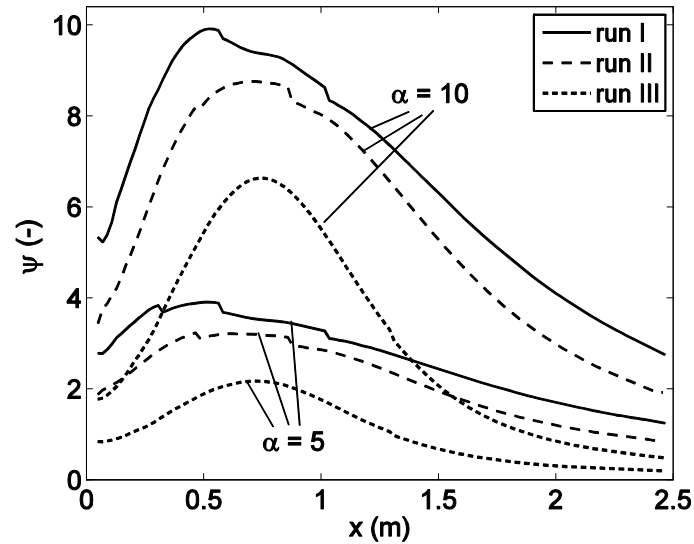


Figure 4.15. Computed values of bed stability parameter  $\Psi$  downstream of the gate for two different values of turbulence impact parameter  $\alpha$ . Runs I, II and III are shown.

The plot shows that run I (three gates with constant opening) has the strongest flow impact on the bed material of the three runs irrespective of the choice for  $\alpha$ . The  $\Psi$ -values of run II show that controlling the discharge without opening more gates already has a lower flow impact on the bed. Run III (seven gates with controlled discharge) has the lowest flow impact. All runs reach their maximum flow impact on the bed around the same (limited) distance downstream of the gate. For all runs the general shape of the curves is quite similar for both values of  $\alpha$ , indicating that turbulence is dominant over mean velocity for the flow impact.

Overall the values of the bed stability parameter are somewhat low compared to previous numerical investigations by Erdbrink and Jongeling (2008) and Erdbrink (2009), which could be attributed to the use of the standard k- $\epsilon$  model in this study instead of the RNG k- $\epsilon$  turbulence model used in the two mentioned studies. Choosing higher  $\alpha$  values could compensate the lower TKE. For practical application one should fix  $\alpha$  after calibration in experimental investigations and one should define a threshold value for  $\Psi$  not to be exceeded during operation to be used for measuring the fitness of different flow scenarios.

Turning to the assessment of gate vibrations, a measured range of structural response frequencies would give the reduced velocity number. If response characteristics of the gate would be known, this would yield an estimate of vibration levels. For now, this computation is postponed; in the next chapter such response data will be found experimentally.

Based on the discussed modelling results and flow analysis, it may be decided to implement the discharge scenario of run II, because it gives a lower impact on the bed material than run I – while still ensuring sufficient discharge volume to reach the target lake level.

#### 4.6 Model coupling tests

In the calculation of  $a_{\text{const}}$  at the start of discharge, some value for  $C_D$  is needed. From the second discharge event onwards there is data available from the discharge model on previously achieved discharges. This data computes the discharges more accurately than the system model, because it solves the local flow equations (that include contraction, losses, etc.) and hence works with one value of  $C_D$  for each time step, rather than keeping it constant throughout the discharge event as does the system model.

Six scenarios were tested for using information from the discharge in the system model for estimating  $C_D$ . For each scenario the lake level is updated using the discharge through the structure as computed by the system model. All test runs use five gates ( $m = 5$ ). Table 4.3 and Table 4.4 contain the definitions and the achieved results of the tested coupling scenarios.

Table 4.3. Testing scenarios for model coupling.

scenario	PID discharge control	target level reached?	discharge model results used in system model?	convergence of $C_D$	convergence of $a$	convergence of $Q$
1	off	yes	no	no	no	no
2	off	yes	yes	yes*	no	yes
3	off	yes	yes	no	yes	no
4	off	yes	yes	yes	maybe	yes
5	on	yes	yes	yes*	yes	no
6	on	yes	yes	yes	yes	yes

\* Average values converge.

Table 4.4. Results of testing scenarios.

scenario	opening in system model $a_{SM}$ (m)	opening in discharge model $a_{DM}$ (m)	error $ a_{SM} - a_{DM}  / a_{DM}$ (%)	discharge in system model $Q_{SM}$ ( $m^3/s$ )	discharge in discharge model $Q_{DM}$ ( $m^3/s$ )	error $ Q_{SM} - Q_{DM}  / Q_{DM}$ (%)
1	0.80	1.04	23	270	230	17
2	0.93	1.04	11	270	279	3
3	0.89	0.87	2	284	252	13
4	0.92	1.03	11	269	275	2
5	0.73	0.83	12	229	208	10
6	0.81	0.77	5	231	231.5	0

A good coupling method feeds the system model with enough information to improve its estimates of  $Q_{\text{gate}}$ ,  $a$  and  $C_D$ . Coupling errors are expressed in Table 4.4 as relative differences at the time of maximum head difference in the fourth discharge event. When constant gate openings are applied, the tests show that without updating the discharge coefficient, the system model is unable to make accurate estimates of the required gate opening and discharges.

Testing all scenarios revealed that scenario 6 gives the best results in terms of errors. See Figure 4.16. This alternative offers the best way to control the discharge and at the same time obtain the best possible match between the models. But the price for this is a more complex trimming of the update parameters (three PID gain parameters and  $\alpha$ ) and longer computation time.

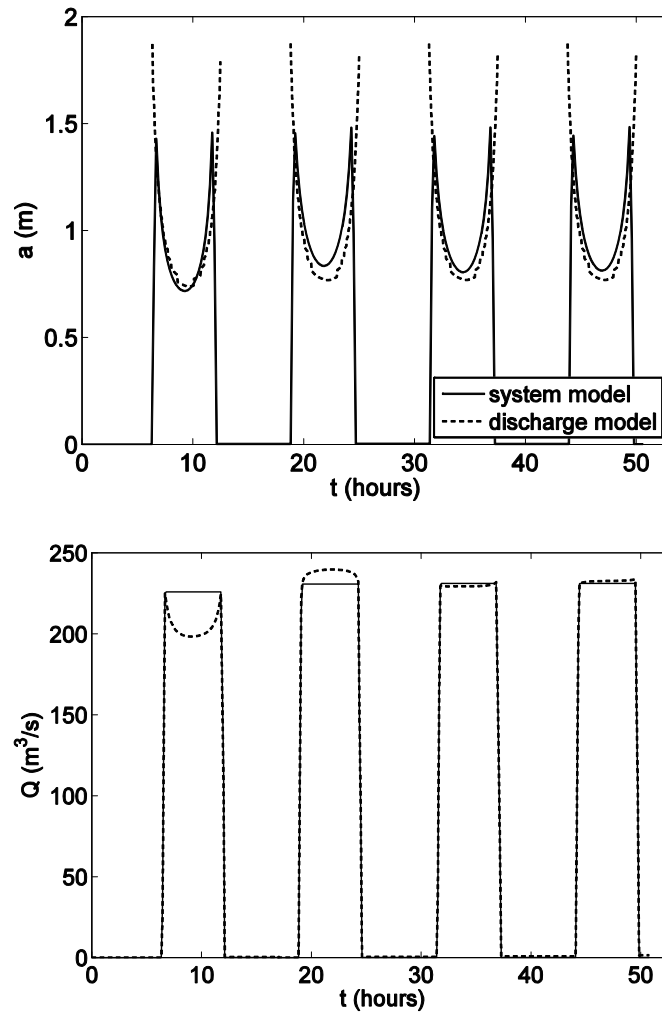


Figure 4.16. Test results of scenario 6. Dotted line indicates discharge model and continuous line indicates system model.

For the choice which scenarios are applied in the main study the ease of parameter trimming and the stability of maximum discharge maxima were considered most important. This led to choosing scenario 2 for the uncontrolled runs and scenario 5 for the controlled runs.

#### **4.7 Conclusions of this chapter**

The described case of a multi-gated outlet barrier sluice has shown how discharge estimates from elementary flow equations and free-surface time-dependent CFD simulations can aid in deciding on optimal gate configuration and opening scenarios. This introduces discharge computations in operational management of hydraulic structures for issues that at present are decided upon by judgement of the operator. The method connects modelling scales with a minimum of data exchange (coupling) and applies a PID-controller to achieve a more constant discharge throughout the entire discharge event under natural head difference. Validation runs showed that the free-surface model produces discharge values for a range of gate openings and submergence levels within an acceptable accuracy of experimental values. Applying PID-control to discharge instead of to water levels is more complicated and requires more gate adjustments (optimisation of this was not investigated here), but it achieves something that PID-control on water levels cannot achieve: control of the flow impact on the structure and its surroundings.